Tandem Electrocatalytic CO_2 Reduction with Efficient Intermediate Conversion over Pyramid-textured Cu-Ag Catalysts

Ya Liu,[†,‡,¶] Haoran Qiu,[†] Jinghan Li,[‡,¶,§] Liejin Guo,[,†] and Joel W. Ager[*,‡,¶]*

[†]International Research Center for Renewable Energy, State Key Laboratory of Multiphase Flow in Power Engineering, Xi'an Jiaotong University, Shaanxi 710049, China

[‡]Joint Center for Artificial Photosynthesis, [¶]Materials Sciences Division, Lawrence Berkeley National Laboratory, Berkeley, California 94720, United States

[§]State Key Laboratory of Metal Matrix Composites, Shanghai Jiao Tong University, Shanghai 200240, China

KEYWORDS: CO_2 reduction, Cu, Ag, electrocatalysis, cascade catalysis

ABSTRACT. If combined with renewably generated electricity, electrochemical CO_2 reduction (E-CO_2R) could be used as a sustainable source of chemicals and fuels. Tandem catalysis approaches are attractive for providing the product selectivity which would be required for commercial application. Here we demonstrate two-step tandem electrocatalytic E-CO_2R with efficient conversion of the intermediate species. The catalyst scaffold is Si (100) which is etched to form a textured surface consisting of micron-sized pyramid structures with {111} facets. Two metals are used in the electrocatalytic cascade: Ag is employed to perform two-electron reduction

of CO_2 to the intermediate CO and Cu performs conversion to more reduced products. Using high angle physical vapor deposition, we form separated, micron-scale areas of the two electrocatalysts on opposite sides of the pyramids, with their relative surface coverages being tunable with deposition angle. Compared to textured scaffolds with blanket Ag and Cu used as controls, bimetallic pyramid tandem catalysts have higher current densities and much lower faradaic efficiencies for CO. These effects are due to efficient conversion of the CO formed on Ag to more reduced products on the Cu. Methane is the main product to be enhanced by the cascade pathway: a bimetallic catalyst with approximately equal coverages of Ag and Cu produces methane with a FE of 62% at -1.1 V_{RHE}, corresponding to a partial current density of 12.7 mA cm^{-2}. We estimate an intermediate conversion yield for the CO intermediate of 80-90%, which is close to the mass-transport limited value predicted by reaction-diffusion simulations.

INTRODUCTION

In future scenarios of abundant and inexpensive electricity generated by sustainable sources such as wind and solar, electrocatalytic CO_2 reduction (E-CO_2R) has the potential to produce fuels and chemicals with a smaller carbon footprint compared to present technologies.[1–8] To this end, many electrocatalysts have been evaluated, both for their selectivity to CO_2R compared to the competing hydrogen evolution reaction (HER) and for their selectivity to C_1, C_2, and C_3 products.[9] Among the few metallic electrocatalysts that favor CO_2 reduction over HER in aqueous conditions, Cu is the only one, so far, known to produce hydrocarbons like CH_4 and C_2H_4 and oxygenates like ethanol and propanol with appreciable faradaic efficiencies (FEs), while others mainly produce two-electron products like CO or formate.[10–16] Although there are recent reports of very high selectivity for certain products, mainly CO, formate, or C_2H_4 using gas diffusion electrodes,[17–22] it is still not possible, in general, to target a specific hydrocarbon product with an E-CO_2R scheme.

Tandem catalysis in which an intermediate species is produced on one catalyst and undergoes further conversion on different catalysts, is a well-established motif in chemical synthesis.[23] In the context of E-CO_2R, CO is an attractive intermediate for cascade catalysis designs, as it can be produced on Au or Ag and can be efficiently reduced on Cu.[16,24–26] Transport of the intermediate species between the different catalyst sites is a key design parameter for tandem catalysts.[27] In bimetallic nanoparticles, surface diffusion or "spill-over" has been posited as the intermediate transport mechanism, and there is ample evidence that cascade processes on the nanoscale can be used to modify the CO_2R product distribution.[28–30] Morales-Guio and co-workers deposited Au nanoparticles on a flat polycrystalline Cu foil and improved the selectivity of oxygenates by creating a high CO concentration on nearby Cu.[28] Using a similar geometry, Zhang *et al.* reported that CO generated on Ag can migrate to surface Cu sites and produce CH_4 via spill-over.[29] Ren *et al.* showed that an *in situ* source of CO is essential for promoting ethanol over the predominant C_2 product ethylene on Zn-Cu nanoparticle catalysts.[31,32] We do note that similarly constructed bimetallic nanoparticles have been reported to favor different products. For example, while Cu-Ag nanoparticles described by Buonsanti and co-workers have improved C_2H_4 and increased overall CO_2R activity compared with control Cu nanoparticles,[27] Yeo and co-workers find that increasing the local CO activity due to its production on Ag opens an alternative catalytic pathway that favors ethanol instead of ethylene.[33] Finally, Meyer and co-workers have reported that ultra-small Ag-Cu nanoparticle catalysts are selective for acetate production.[34]

Intermediate transport via diffusion can also be used in cascade E-CO_2R provided that distance between catalyst sites is less than the typical thickness, *ca.* 100 μm, of the diffusion layer which forms at the surface of the electrocatalyst. For example, Lum and Ager created a tandem cascade using micropatterned Ag and Cu lines and found that their relative areal densities controlled the

product distributions, with C_2 and C_3 oxygenates being favored at low Cu coverages.[35] Convective transport can be used to transport intermediates over longer distances. Gurudayal *et al.* demonstrated a sequential cascade pathway on the mm scale in a continuous flow reactor with an upstream Ag electrode and a downstream Cu electrode; it was found that the CO produced by the upstream electrode affected the product distribution produced by the downstream Cu.[36] In a demonstration that accessed still larger length scales for intermediate transport, Spurgeon and co-workers pumped electrolyte from one reactor to another to realize a two-step cascade for ethanol synthesis.[37]

Examining this literature we find that tandem cascade designs with micron-scale design features remain relatively unexplored. At this length scale, diffusional transport is possible, provided that the distance between sites in the cascade is less than the diffusion layer thickness. At the same time, spillover might also be possible. Although the CO diffusion coefficient on metals in the aqueous electrochemical environment has not been well explored, CO diffusion behavior on Pt in the electrolyte may provide some insight. In studies performed in the context of fuel cell catalysis, Wieckowski and co-workers found that the CO diffusion length on Pt and Pt/Ru is on the order of 10's of nm per second, depending on the CO coverage and the particle sites.[38] Using the proposed linear relationship of the energy barrier for diffusion with the adsorbate binding energy as a guide,[39] we might expect faster diffusion of CO on Cu and Ag due to their weaker binding energy compared to Pt. On the other hand, recent first principle calculations show that the CO binding energy on Cu is increased at the relatively large negative potentials used in electrochemical CO_2 reduction,[40] which would lead to slower diffusion. This is consistent with the observation of differences in isotope fractions found in C_2 products produced on some Cu surfaces by a mixed ^{13}CO-$^{12}CO_2$ feed.[41] This analysis motivates us to hypothesize that very efficient intermediate

conversion may be achieved in cascades constructed on the micron scale, as, potentially, both surface diffusion and diffusion through the electrolyte could contribute.

To test this hypothesis, we used textured Si wafers with pyramid structures having the desired length scale in the 10-micron range. By varying the deposition angle used in the physical vapor deposition we controlled the location of the electrocatalysts: normal incidence for blanket coverage and higher deposition angles for selective deposition on the sides of the pyramids, as illustrated in Figure 1. Bimetallic catalysts are made by blanket coverage of one metal followed by high angle deposition of the other. The texturing process exposes {111} Si facets and we expected that the deposited metals will have a similar orientation,[42] although the evaluation of the surface orientation with CV scans was not definitive (Figure S14). In the case of Cu, we would expect that the {111} orientation may favor the production of methane as C-C coupling has a higher barrier on this surface compared to {100}.[43] When operated in CO_2-saturated bicarbonate buffer, single metal textured controls produce the expected products: e.g. > 80% FE for CO near -1.1 V_{RHE} for Ag and a mixture of C_1 and C_2 products with methane as the main product in the same potential range for Cu. When operated at a potential at which both Ag and Cu are active, we find that textured bimetallic catalysts have a much lower FE towards CO and a higher current density for CO_2R, both of which point to a cascade pathway. The estimated conversion efficiency of CO generated on Ag on Cu is as high as 89% and approaches the mass transport limit.

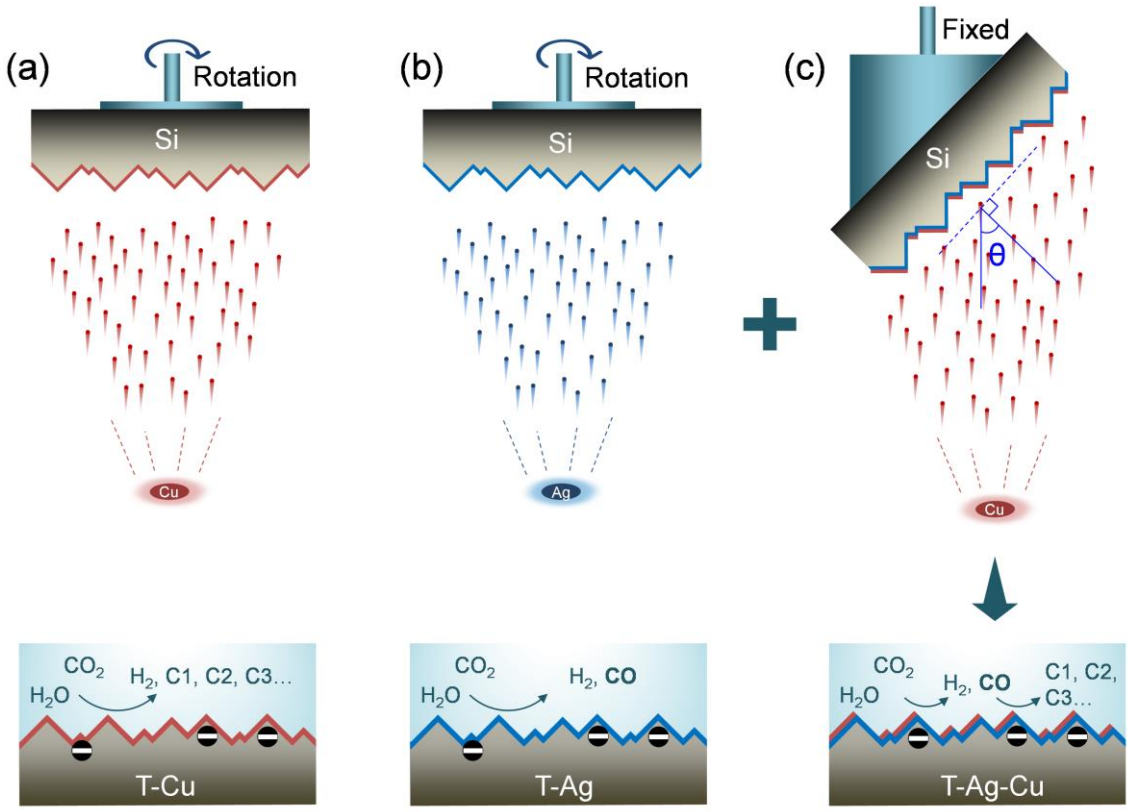


Figure 1. **Fabrication procedure for bimetallic catalysts.** Textured Si wafers are used as scaffolds for fabrication of CO_2R electrocatalysts. Physical vapor deposition at normal incidence produces a blanket coverage of **(a)** Cu (sample designation T-Cu) or **(b)** Ag (sample designation T-Ag). Blanket deposition of Ag **(b)** followed by high angle deposition of Cu **(c)** leads to deposition of Cu on one side of the pyramids, with the other side being shaded (sample designation T-Ag-Cuθ, where θ is tilt angle).

METHODS

Fabrication of electrocatalysts. The detailed fabrication procedures are provided in the Supporting Information; a brief overview is presented here. Catalyst scaffolds were formed by etching (100) n-type silicon wafers in aqueous KOH at 78 °C; due to the different etching rates between {100} and {111} planes in silicon a pyramidal structure can be formed.[44] Blanket

deposition of Ag or Cu was performed by electron beam evaporation at normal incidence with the substrate rotating to form a uniform coating (~ 100 nm), as shown in Figures 1a and 1b. These pyramid-textured electrodes are denoted T-Cu and T-Ag, respectively. For textured bimetallic catalysts, Ag was deposited at normal incidence followed by Cu deposition (~100 nm) with the substrate fixed at a tilt angle θ, as shown in Figure 1c. These samples are denoted T-Ag-Cuθ. With this high-angle deposition method, Cu is deposited only on one side of the pyramids, leaving the previously deposited Ag on the other side exposed. By changing the deposition angle θ, the relative surface ratio between the two metals can be easily controlled. To make untextured electrodes used as additional controls, Cu was directly deposited on a polished n-type wafer using the same procedure as for T-Cu. Table S1 is a list of all electrocatalysts used in the study. After the deposition of catalysts, a thick layer of Au (~200 nm) and a thin layer of Ti (~10 nm) were deposited on the backside of wafers to produce an ohmic contact between the wafer and working electrode lead (Figure S1). Samples were also made by Cu deposition on clean (100) n-type silicon wafers for use as controls; these samples are denoted as F-Cu.

Surface characterization. Surface morphology was evaluated by a JEOL JSM-7800F field emission scanning electron microscope (FE-SEM). Relative surface coverages of Ag and Cu were determined using energy-dispersive X-ray spectroscopy (EDS) installed in the FE-SEM (OXFORD INCA). Image processing software (Adobe Photoshop) was used to calculate the coverage ratios based on the coverage of the surface obtained by the EDS measurements. The detachment rate of bubbles was compared between flat and textured catalysts by measuring the adhesive force of the bubbles to the surface using a high-sensitivity tensiometer from Dataphysics DCAT 25, Germany.

Electrochemical CO_2R measurements. A Biologic SP-300 potentiostat was used for all electrochemical measurements reported here. CO_2R was carried out using a self-designed H-cell sealed with Teflon O-rings, as shown in Figure S2. The as-prepared electrode was then sealed with silver conductive paint (Structure Probe, Inc.), two-part epoxy (3M), and Cu wire before used as working electrode. Silver/silver chloride (Ag/AgCl), and a platinum wire served as reference and counter electrodes, respectively. The electrolyte was CO_2-saturated aqueous 0.2 M $KHCO_3$, (pH 6.9). A Selemion AMV anion exchange membrane was employed to separate the electrolyte in the cathode and anode chambers. The measured potential *vs.* the Ag/AgCl reference electrode was converted to the reversible hydrogen electrode (RHE) scale using the formula $V_{RHE} = V_{Ag/AgCl} + 0.059\ pH + 0.1976\ V$. 85% of the solution resistance (R_u) was *in-situ* compensated and the remaining 15% was post-corrected after the experiment (Figure S3).

Product analysis. A previously reported procedure was used for product quantification.[45] All of the gas products (H_2, CO, CH_4, C_2H_6, and C_2H_4) were online analyzed by using a MG#3 Gas Chromatograph (GC) from SRI Instruments, which equipped with a 12" long HaySep D column. Hydrogen was detected by a thermal conductivity detector (TCD), while the hydrocarbons were detected by a flame ionization detector (FID). The gas products were carried by CO_2 and purged in GC continuously. Each CO_2R experiment was carried out for 67 minutes, and the gas products were tested at 5, 20, 35, 50, and 65 min after starting a run. The values from the last three measurements were averaged to produce the reported data.

The liquid products were collected after electrolysis and analyzed by a High-Performance Liquid Chromatograph (HPLC) from Thermo Scientific (UltiMate 3000) The column used in this HPLC was an Aminex HPX 87-H from Bio-Rad, and the liquid products (including glyoxal, glycolaldehyde, formate, formaldehyde, acetate, ethylene glycol, hydroxyacetone, acetaldehyde,

methanol, allyl alcohol, ethanol, propionaldehyde, and n-propanol) were detected by a refractive index detector (RID). 1 mM diluted sulfuric acid was used as the eluent, and 10 μL of the sample was injected into the column.

Mass transport simulations. The CO concentration contours for T-Ag-Cu were calculated with the finite element software, COMSOL (see the Supporting Information for full modeling details). 3-dimensional modeling was carried on the minimum repeat units within pyramid-textured Cu-Ag bimetallic catalysts. Table S3 contains a detailed parameter list. A flux boundary condition was set at the Ag surface, 2.36×10^{-7} mol cm^{-2} s^{-1}, which is equivalent to the experimentally measured partial current density of 4.55 mA cm^{-2} measured at -1.1 V_{RHE}. To determine the mass transfer limiting condition, the flux boundary condition at the surface of the Cu was set to a value that produces a minimum (but still positive) concentration of CO at the surface, see SI for details. A zero concentration boundary condition is set at the boundary between the Nernst layer and the bulk (located at a distance of 100 μm from the tips of the pyramids) such that diffusion of CO to the Cu and to the bulk compete against each other.

RESULTS AND DISCUSSION

Pyramid-textured electrodes: T-Ag, T-Cu, and T-Ag-Cu. The Si scaffolds formed by the texturing process are shown in Figures 2a and 2b. The scaffolds have <111>-oriented surfaces with an angle of 90º between opposite edges, forming pyramids with faces oriented at 54.7º with respect to the substrate normal (inset of Figure 2b). The pyramids vary in size: the largest pyramids have a base width of up to 30 μm whereas smaller pyramids are a few microns in size.

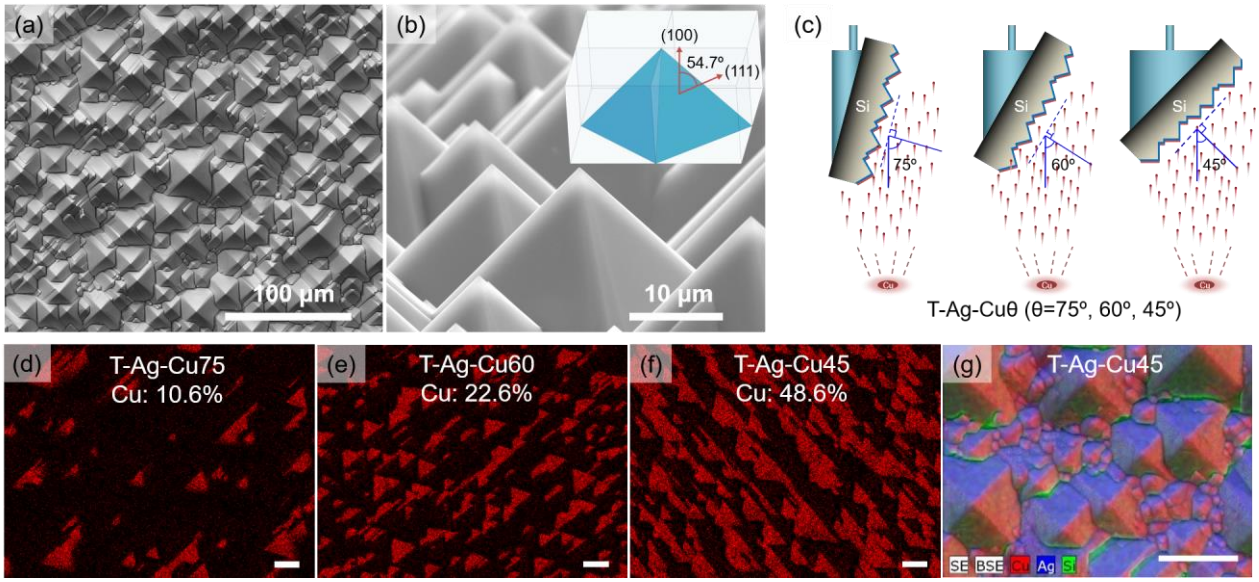


Figure 2. Textured morphology and Coverage control. (a) Top view and **(b)** angle view SEM images of the pyramid-textured n-type silicon wafer after wet etching. The inset of **(b)** shows geometric relationships of the edges and surfaces on a single pyramid. **(c)** Method used for relative surface coverage control. Decreasing the substrate tilt angle θ from 75º to 45º increases the Cu coverage. **(d-f)** Cu distribution (red shading) on samples T-Ag-Cu75, T-Ag-Cu60, and T-Ag-Cu45. **(g)** Integrated EDS mapping with all elements Cu (red), Ag (blue), and Si (green). Scale bar d-g 10 μm.

Figure 2c depicts the method used to control the relative coverage of Cu in textured Ag-Cu catalysts. High deposition angles for Cu lead to significant shadowing, as shown in Figure 2d for a substrate tilt angle θ = 75º (see Figure S4 for a detailed illustration of the shadowing effect). At this angle, the Cu is preferentially deposited on the tops of the pyramids and the relative Cu coverage is 10.6%. Reducing θ increases the areal coverage of Cu, as shown in Figures 2e and 2f for 60º (22.6%) and 45º (48.6%). Figure 2g shows the approximately even coverage of Ag and Cu produced for θ = 45º with the Ag and Cu located on opposite sides of the pyramids with typical

dimensions on the *ca.* 10 μm scale. Figures S5-S8 contain further details on the measurement of the areal coverages and evaluation of the catalyst morphology.

CO_2R with T-Ag and T-Cu controls. Linear sweep voltammograms (LSVs) for textured single metal controls T-Ag and T-Cu performed in CO_2 saturated 0.2 M $KHCO_3$ are shown in Figure 3a. Compared with T-Cu, T-Ag has a more negative onset potential and a lower current density throughout the measurement range (current densities were stable over the ~1 hr evaluation period, Figures S11 and S13c). We considered the possibility that differences in roughness may also affect the CO2R performance.[46] AFM measurements show that the surface roughnesses for T-Ag and T-Cu are similar (12.18 and 12.25 nm, respectively, Figure S9), ruling out this effect in our case. Product distributions were evaluated in the range -1.0 - -1.4 V_{RHE} for T-Ag (Figure 3bc) and -0.8 - -1.2 V_{RHE} for T-Cu (Figure 3def). For pyramid-textured Ag, as shown in Figure 3b, the main product is CO within this range, reaching an FE of 87% at -1.1 V_{RHE}. At more negative potentials, the selectivity to formate increases at the expense of CO[47]. Significant FE for the competing reaction hydrogen evolution reaction (HER) begins at around -1.3 V_{RHE} and becomes the dominant reaction when a further negative potential is applied. Very small amounts (FE < 1%) of hydrocarbons and carbohydrates were also detected, Figure 3c. Untextured controls F-Cu were also evaluated, Figure S12. An interesting effect was found at high current densities (> 50 mA cm^{-2}); chronoamperometry data for the textured catalysts was less noisy than for flat substrates with the same catalyst, Figure S13. The effect is attributed to more facile bubble detachment from the textured catalyst (the bubbles are likely H_2 at these high current densities), as demonstrated by adhesive force measurements shown in Figure S10.

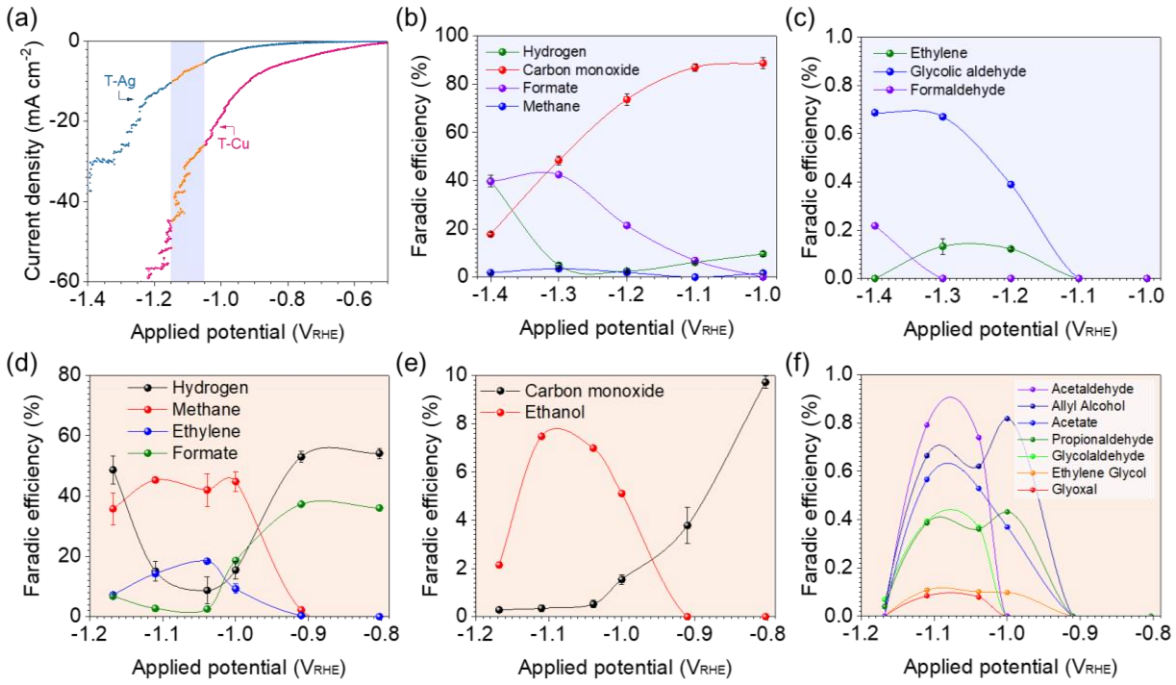


Figure 3. Comparison of textured controls. (a) LSVs for T-Ag and T-Cu. Product distributions for T-Ag: **(b)** H_2, CO, formate and methane and **(c)** minor C_2 products. FE for CO on T-Ag is 80% near -1.1 V_{RHE}. Product distributions for T-Cu: **(d)** H_2, methane, ethylene and formate; **(e)** CO and ethanol; **(f)** minor C_2 products.

For T-Cu CO and formate are the main CO_2R products at -0.8 V_{RHE} with a concomitant H_2 production with an FE higher than 50%. With increasing overpotential, C_1-C_3 products appear and the FEs for 2-electron products, CO and formate, and for H_2 are reduced. At -1.2 V_{RHE} the FE for H_2 increases, which may be an indication of a mass transfer limit. In the range -0.9 - -1.1 V_{RHE}, methane is the main CO_2R product with an FE of 40-60%, consistent with what might be expected from {111} surfaces of Cu (the orientation of the prepared Cu on T-Cu is suggested by cyclic voltammetry, Figure S14). The FE for CO on T-Cu decreases with increasing overpotential and is very low, <1% at potentials more negative than -1 V_{RHE}. This implies that Cu at this potential facilely converts CO to more reduced products, which has been reported before in CO reduction

studies performed under similar conditions.[48] We thus expect that additional CO which could be provided to the Cu catalysts for the T-Cu-Ag catalyst could also be further reduced. Finally, it is interesting that the ratio of the current densities of T-Cu is ~ 1.73 times of that flat Cu (F-Cu) under the same applied potential, which is in close correspondence with the relative ratios of their surface areas calculated from a geometrical analysis of the pyramid shape (Figure S13). The electroactive surface area measurements indicate that the calculated roughness factor (F-Cu is set to 1) of the pyramid-textured electrodes lie in a range from 1.62 to 1.84, which we do not view as being significantly different from 1.73 (Figure S15 and Table S2).

Non-interacting bimetallic model. It informs the analysis of the experimental data for the textured bimetallic catalysts presented below to consider what would be expected in the limit of zero transport of CO between Ag, where it is produced, and Cu, where it could be consumed. In this simplified case, the catalysts would act independently of each other, and the predicted current density j_x for a given areal coverage of Cu (x) would be given by a simple linear interpolation between values measured for the single metal controls:

$$j_x = (1 - x)j_{Ag} + xj_{Cu}, \quad (1)$$

where j_{Ag} is the measured current density of T-Ag and j_{Cu} is the measured current density of T-Cu. The FE for a given product in the limit of non-interacting catalysts would be:

$$FE_{x_i} = \frac{(1-x)j_{Ag}FE_{Ag_i}+xj_{Cu}FE_{Cu_i}}{(1-x)j_{Ag}+xj_{Cu}}, \quad (2)$$

where FE_{x_i} is the predicted faradic efficiency of product i on a pyramidal bimetallic catalyst with Cu coverage x, FE_{Ag_i} is the faradic efficiency of product i on T-Ag, and FE_{Cu_i} is the faradaic efficiency on T-Cu.

CO_2R for textured Cu-Ag Catalyst. LSV curves for the three pyramid textured Cu-Ag catalysts are shown in Figure 4a. Overall, they are similar to each, with the current densities for T-

Ag-Cu45 being slightly larger, as might be expected from its relatively higher Cu coverage. The current densities of all of the bimetallic catalyst are lower than that of T-Cu, the control case with blanket Cu coverage (Figure 3a). Again, this is expected as T-Ag control catalyst has a lower current density than T-Cu. Still, the current density for all of the bimetallic catalysts is higher than the prediction of the non-interacting model, as shown in Figure 4b.

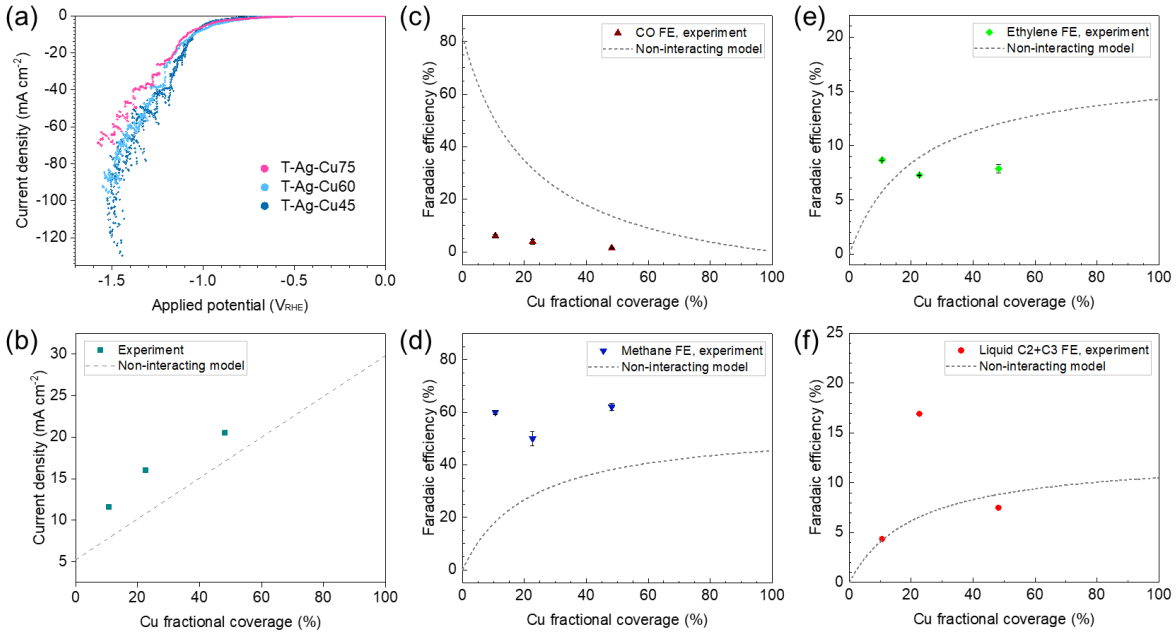


Figure 4. CO_2R performance on T-Ag-Cu and their comparison with the non-interacting model. (a) LSVs for T-Ag-Cu with different deposition angles. **(b)** Observed current densities obtained at -1.1±0.05 V_{RHE} for bimetallic textured electrodes as a function of fractional Cu coverage. Dashed line is for a model which assumes that the Ag and Cu act independently and do not interact, Eq. (1). Experimental current densities are clearly higher than predicted by the non-interacting model. **(c-f)** Observed Faradaic efficiencies for **(c)** CO, **(d)** methane, **(e)** ethylene and **(f)** liquid C_2 and C_3 oxygenates obtained at -1.1 V_{RHE} in CO_2-saturated 0.2 M $KHCO_3$, as a function of fractional Cu coverage for the bimetallic textured electrodes (see Figures S16-21 for precise potentials, FEs and partial current densities for individual liquid products, comparison with the

non-interacting model in terms of partial current densities, results for other potentials, and a 12-hour stability evaluation). Dashed lines are from a model which assumes independent behavior of the Ag and Cu regions, Eq. (2).

Comparison of the product distributions obtained at -1.1±0.05 V_{RHE} reveals more striking deviations from the non-interacting model. If there were no interactions between the Ag and Cu, the CO production should increase dramatically with the decreased Cu coverage, as shown by the dashed line in Figure 4c. However, the observed FEs for CO on T-Ag-Cu are in the range of only 1.5-6.1%, with only a small increasing trend as the Cu coverage is decreased. Similarly, large deviations from the non-interacting model are found in the product distributions. The yield of methane from the textured bimetallic catalysts is higher than for the T-Cu and much higher than predicted by the non-interacting model, Figure 4d. As a specific example, T-Ag-Cu75 has an areal Cu coverage of only 10.6% but has a FE towards methane of 60%, more than three times the predicted value of 18% and higher than the T-Cu control which has an FE of 45%. The highest partial current density for methane production among the tested bimetallic samples is T-Ag-Cu45, which is 12.7 mA cm^{-2}, with a total current density of 20.5 mA cm^{-2}. As the non-interacting model is in poor agreement with the experimental data, we conclude that there is significant interaction between the Ag and Cu on producing CH_4, which will be discussed below.

As the FEs for HER on the bimetallic catalysts are all <20% (Figure S16), the increase in CH_4 FE comes at the expense of other CO_2R products. Figure 4e shows that the experimental FEs for C_2H_4 for the bimetallic catalysts are about 8%, lower than the *ca*. 15% observed for the T-Cu control. Figure 4f examines the FEs for liquid oxygenate products, mainly ethanol and acetaldehyde (see Figure S16 for details). While there is an apparent increase for these products compared to the non-interacting model for one case, T-Ag-Cu60, a clear trend was difficult to

discern. In other studies invoking a CO spillover mechanism, C_2 products are often favored, whereas the C1 product methane is enhanced here. It is possible that the depositing Cu only on the facets of the <111>-oriented pyramids increases the fraction of Cu{111} surface planes and hence leads to a preference for C_1 products.

Estimate of intermediate conversion efficiency. We take the reduced FE for CO and the enhanced FE for CH_4 for the bimetallic textured catalysts, compared to a non-interacting model and the CO2R performance of T-Ag and T-Cu, to be strong evidence of efficient conversion of CO produced on the Ag, consistent with a tandem cascade catalysis scheme. Mass transport simulations were employed to evaluate the conversion efficiency of the CO intermediate. Figure 5a shows CO concentration contours (false color) and diffusion fluxes (white lines with arrows) for geometries corresponding to the three textured bimetallic catalysts in the study and for the T-Ag and T-Cu controls. The close proximity, *ca.* 10 μm of the Cu sink to the Ag source compared to the width of the diffusion layer, assumed to be 100 μm,[45,49] leads to predictions of very high conversion efficiencies, over 94%, in the limit of mass transfer limited consumption at the Cu. The mathematical modeling provides an upper limit to the CO intermediate conversion with the pyramid structure. It is also notable that the predicted CO concentration near the surface does not exceed 1 mM, the CO solubility limit, except for the T-Ag-Cu75 case with the smallest Cu coverage. This is important as CO bubble nucleation, which has been observed previously in CO_2R cascades employing CO as an intermediate,[36] might be expected to reduce the conversion efficiency. As a contrast, the CO concentration contours of the three textured bimetallic catalysts for the non-interacting model are shown in Figure S23.

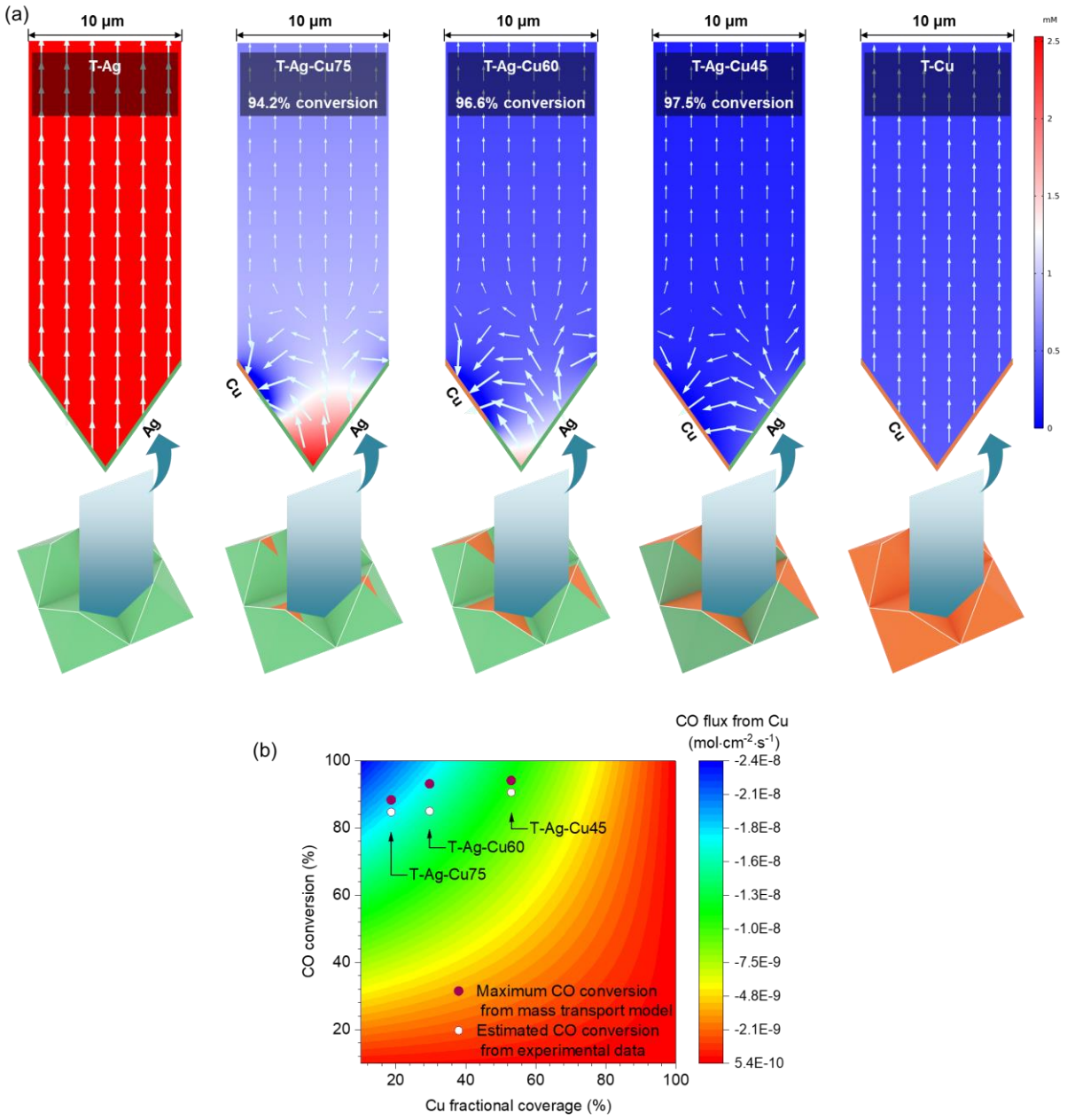


Figure 5. Mass transport modeling and comparison to experiment. (a) CO concentration contours for the cross-section of adjacent pyramids. The insets at the bottom show the pyramids: the orange areas are Cu and the green regions are Ag. Above are shown 2-dimensional contour plots of CO concentration derived from the 3-dimensional modeling carried on a minimum repeat unit (the areas inside of the white dashed boxes, see also Figure S22). A current density of 4.55 mA cm^{-2} for the formation of CO on the Ag was assumed and mass transfer-limited conditions

were determined at the surface of Cu to define an upper limit for intermediate conversion (see SI for complete model details). The CO flux from Cu was set at -6.70×10^{-8} mol cm^{-2} s^{-1}, -4.15×10^{-8} mol cm^{-2} s^{-1}, and -2.15×10^{-8} mol cm^{-2} s^{-1} for T-Ag, T-Ag-Cu75, T-Ag-Cu60, T-Ag-Cu45, and T-Cu, respectively. The white arrows indicate CO flux. **(b)** CO conversion from the simulations (red dots) and estimated from Eq. (3) for the experimental data (white dots) as a function of Cu coverage. The contours denoting the CO flux at the Cu are obtained from Eq. (4).

The non-interacting model discussed above can be used to estimate the experimental CO conversion η_{CO} for a bimetallic catalyst with an areal coverage of *x* by comparing the measured CO flux, $FE_{Co,x}j_x$, corrected for the small amount of CO produced by Cu by itself, $xj_{Cu}FE_{CO,Cu}$, to the predicted flux from Ag if there were no subsequent reaction on Cu, $(1-x)\,j_{Ag}FE_{CO,Ag}$:

$$\eta_{CO}(x) = 1 - \frac{FE_{Co,x}j_x - xj_{Cu}FE_{CO,Cu}}{(1-x)\,j_{Ag}FE_{CO,Ag}} \tag{3}$$

For any conditions between the non-interacting and the upper limit models, the flux of CO from Cu for pyramid-textured Cu-Ag catalysts, $N_{CO}Cu$, can be calculated via a flux balance between the CO flux from Cu by itself, N_{CO}(T-Cu) and the converted CO from Ag, $((1-x)/x)\cdot\eta_{CO}\cdot N_{CO}$(T-Ag).

$$N_{CO}Cu = N_{CO}(\text{T-Cu}) - \frac{(1-x)}{x}\cdot\eta_{CO}\cdot N_{CO}(\text{T-Ag}) \tag{4}$$

As shown in Figure 5b, at low Cu fractional coverage a high CO flux from Cu is required to reach significant CO conversion efficiencies. For the experimental condition, the CO conversion efficiencies estimated from Eq. (3) are all above 80%. There is a slight trend of increasing conversion efficiency with increasing Cu coverage, with the CO conversion of T-Ag-Cu45 reaching 89%. These values are higher than values estimated using a similar analysis for a cascade using interdigitated Ag and Cu at a spacing of *ca.* 30 μm;[35] we attribute the higher conversion

efficiency in this work to the smaller average distance between the catalyst sites, which increases the efficiency of diffusional transport.

However, there are tradeoffs between these two cascade approaches. In the interdigitated cascades, much larger CO activities were predicted by the modeling, and these were thought to be responsible for the high yield of oxygenates found at smaller areal coverages of Cu. Here, the local CO concentration is predicted to be smaller and, as discussed above, the catalyst fabrication method could favor {111} faceting. Both of these factors would contribute to the enhancement of methane found here for the cascade pathway instead of the C_2 oxygenates found in prior work.

Finally, we consider whether diffusion through the electrolyte or surface diffusion (or both) is responsible for the high CO conversion efficiencies found experimentally. Referring to Figure 5a, it is possible to rationalize the experimental results with diffusion through the electrolyte only, as the observed values are smaller than the mass transfer limit. Referring to Figures 2d-f, catalysts with lower Cu coverage have, on average, smaller mean Ag-Cu site spacings, which would be favorable for the spillover mechanism. The experimental data shown in Figure 5b have a small upward trend with increasing Cu coverage in the direction predicted by the mass transfer model. This small trend is in the opposite direction of what might be expected from a pure spillover effect. Still, we cannot rule out the possibility that both effects might be occurring in the textured bimetallic catalysts, and, given the overall very high conversion values, it will be difficult to discern them with this type of design. It may be necessary to physically separate the Cu and Ag domains on this length scale with a surface diffusion barrier to further elucidate the mechanism.

CONCLUSIONS

We have demonstrated a simple method to create bimetallic CO_2R electrocatalysts with well-defined geometries on pyramid-textured scaffolds. A well-known procedure creates *ca.* 10 μm

sized pyramids with exposed {111} facets on [100]-oriented Si wafers. Blanket deposition of one metal using physical vapor deposition at normal incidence followed by high angle deposition of a second metal creates a bimetallic catalyst with the two metals situated on opposite sides of the pyramid. The relative coverage of the second metal can be controlled with the deposition angle. The Ag-Cu bimetallic catalysts function as a tandem cascade, with efficient conversion of the CO made on the Ag to methane on Cu. The fabrication method shown here can be generalized to other metals or materials amenable to physical vapor deposition, and could potentially be used to make bimetallic photocathodes for light-driven CO_2 reduction.

ASSOCIATED CONTENT

Supporting Information. Synthesis procedures; electrochemical measurement details; supplemental structural characterization; supplemental electrochemical data; simulation details.

AUTHOR INFORMATION

Corresponding Authors

lj-guo@mail.xjtu.edu.cn, JWAger@lbl.gov

Author Contributions

The manuscript was written through contributions of all authors. All authors have given approval to the final version of the manuscript.

ACKNOWLEDGMENT

We thank Peter Lobaccaro and Yanwei Lum for assistance with product analysis, Jeffrey W. Beeman for construction of the substrate holder, Shengjie Bai for assistance with adhesion force measurements, and Xiaojie Xu and Sudhanshu Shukla for helpful discussions. SEM, EDS, e-beam

evaporation, and CO_2R product analysis were supported by the Joint Center for Artificial Photosynthesis, a DOE Energy Innovation Hub, supported through the Office of Science of the U.S. Department of Energy under Award No. DE-SC0004993. FESEM, EDS, and adhesion force measurements were supported by National Natural Science Foundation of China (Nos. 51888103 and 51906199). Wet etching was performed in the Electronic Materials Program, which is supported by the Director, Office of Science, Office of Basic Energy Sciences, Materials Sciences and Engineering Division, of the U.S. Department of Energy under Contract No. DE-AC02-05CH11231. Y.L. acknowledges fellowship support from the Initiative Postdocs Supporting Program. J.L. acknowledges financial support from the China Scholarship Council.

REFERENCES

(1) Gattrell, M.; Gupta, N.; Co, A. Electrochemical Reduction of CO_2 to Hydrocarbons to Store Renewable Electrical Energy and Upgrade Biogas. *Energy Convers. Manag.* **2007**, *48* (4), 1255–1265.

(2) Graves, C.; Ebbesen, S. D.; Mogensen, M.; Lackner, K. S. Sustainable Hydrocarbon Fuels by Recycling CO_2 and H_2O with Renewable or Nuclear Energy. *Renew. Sustain. Energy Rev.* **2011**, *15* (1), 1–23.

(3) Spurgeon, J. M.; Kumar, B. A Comparative Technoeconomic Analysis of Pathways for Commercial Electrochemical CO_2 Reduction to Liquid Products. *Energy Environ. Sci.* **2018**, *11* (6), 1536–1551.

(4) Bushuyev, O. S. S.; De Luna, P.; Dinh, C. T. T.; Tao, L.; Saur, G.; van de Lagemaat, J.; Kelley, S. O. O.; Sargent, E. H. H. What Should We Make with CO_2 and How Can We Make It? *Joule* **2018**, *2* (5), 825–832.

(5) Jouny, M.; Luc, W.; Jiao, F. General Techno-Economic Analysis of CO_2 Electrolysis Systems. *Ind. Eng. Chem. Res.* **2018**, *57* (6), 2165–2177.

(6) Shih, C. F.; Zhang, T.; Li, J.; Bai, C. Powering the Future with Liquid Sunshine. *Joule* **2018**, *2* (10), 1925–1949.

(7) Artz, J.; Müller, T. E.; Thenert, K.; Kleinekorte, J.; Meys, R.; Sternberg, A.; Bardow, A.; Leitner, W. Sustainable Conversion of Carbon Dioxide: An Integrated Review of Catalysis and Life Cycle Assessment. *Chem. Rev.* **2018**, *118* (2), 434–504.

(8) Martín, A. J.; Pérez-Ramírez, J. Heading to Distributed Electrocatalytic Conversion of Small Abundant Molecules into Fuels, Chemicals, and Fertilizers. *Joule* **2019**, *3* (11), 2602–2621.

(9) Hori, Y. Electrochemical CO_2 Reduction on Metal Electrodes. In *Modern Aspects of Electrochemistry*; Springer New York: New York, NY, 2008; Vol. 29, pp 89–189.

(10) Yoshio, H.; Katsuhei, K.; Shin, S. Production of CO and CH_4 in Electrochemical Reduction of CO_2 at Metal Electrodes in Aqueous Hydrogencarbonate Solution. *Chem. Lett.* **1985**, *14* (11), 1695–1698.

(11) Nitopi, S.; Bertheussen, E.; Scott, S. B.; Liu, X.; Engstfeld, A. K.; Horch, S.; Seger, B.; Stephens, I. E. L. L.; Chan, K.; Hahn, C.; Nørskov, J. K.; Jaramillo, T. F.; Chorkendorff, I. Progress and Perspectives of Electrochemical CO_2 Reduction on Copper in Aqueous Electrolyte. *Chem. Rev.* **2019**, *119* (12), 7610–7672.

(12) Dinh, C.-T.; Burdyny, T.; Kibria, M. G.; Seifitokaldani, A.; Gabardo, C. M.; García de Arquer, F. P.; Kiani, A.; Edwards, J. P.; De Luna, P.; Bushuyev, O. S.; Zou, C.; Quintero-Bermudez, R.; Pang, Y.; Sinton, D.; Sargent, E. H. CO_2 Electroreduction to Ethylene via Hydroxide-Mediated Copper Catalysis at an Abrupt Interface. *Science.* **2018**, *360* (6390), 783–787.

(13) Gabardo, C. M.; Seifitokaldani, A.; Edwards, J. P.; Dinh, C. T.; Burdyny, T.; Kibria, M. G.; O'Brien, C. P.; Sargent, E. H.; Sinton, D. Combined High Alkalinity and Pressurization Enable Efficient CO_2 Electroreduction to CO. *Energy Environ. Sci.* **2018**, *11* (9), 2531–2539. https://doi.org/10.1039/c8ee01684d.

(14) Back, S.; Yeom, M. S.; Jung, Y. Active Sites of Au and Ag Nanoparticle Catalysts for CO_2 Electroreduction to CO. *ACS Catal.* **2015**, *5* (9), 5089–5096.

(15) Chen, Y.; Li, C. W.; Kanan, M. W. Aqueous CO_2 Reduction at Very Low Overpotential on Oxide-Derived Au Nanoparticles. *J. Am. Chem. Soc.* **2012**, *134* (49), 19969–19972.

(16) Liu, M.; Pang, Y.; Zhang, B.; De Luna, P.; Voznyy, O.; Xu, J.; Zheng, X.; Dinh, C. T.; Fan, F.; Cao, C.; de Arquer, F. P. G.; Safaei, T. S.; Mepham, A.; Klinkova, A.; Kumacheva, E.; Filleter, T.; Sinton, D.; Kelley, S. O.; Sargent, E. H. Enhanced Electrocatalytic CO_2 Reduction via Field-Induced Reagent Concentration. *Nature* **2016**, *537* (7620), 382–386.

(17) Verma, S.; Hamasaki, Y.; Kim, C.; Huang, W.; Lu, S.; Jhong, H.-R. M.; Gewirth, A. A.; Fujigaya, T.; Nakashima, N.; Kenis, P. J. A. Insights into the Low Overpotential Electroreduction of CO 2 to CO on a Supported Gold Catalyst in an Alkaline Flow Electrolyzer. *ACS Energy Lett.* **2018**, *3* (1), 193–198.

(18) Salvatore, D. A.; Weekes, D. M.; He, J.; Dettelbach, K. E.; Li, Y. C.; Mallouk, T. E.; Berlinguette, C. P. Electrolysis of Gaseous CO_2 to CO in a Flow Cell with a Bipolar Membrane. *ACS Energy Lett.* **2018**, *3* (1), 149–154.

(19) Liu, Z.; Yang, H.; Kutz, R.; Masel, R. I. CO_2 Electrolysis to CO and O_2 at High Selectivity, Stability and Efficiency Using Sustainion Membranes. *J. Electrochem. Soc.* **2018**, *165* (15), J3371–J3377.

(20) Xia, C.; Zhu, P.; Jiang, Q.; Pan, Y.; Liang, W.; Stavitsk, E.; Alshareef, H. N.; Wang, H. Continuous Production of Pure Liquid Fuel Solutions via Electrocatalytic CO_2 Reduction Using Solid-Electrolyte Devices. *Nat. Energy* **2019**, *4* (9), 776–785.

(21) Cheng, W.-H.; Richter, M. H.; Sullivan, I.; Larson, D. M.; Xiang, C.; Brunschwig, B. S.; Atwater, H. A. CO_2 Reduction to CO with 19% Efficiency in a Solar-Driven Gas Diffusion Electrode Flow Cell under Outdoor Solar Illumination. *ACS Energy Lett.* **2020**, acsenergylett.9b02576.

(22) García de Arquer, F. P.; Dinh, C. T.; Ozden, A.; Wicks, J.; McCallum, C.; Kirmani, A. R.; Nam, D. H.; Gabardo, C.; Seifitokaldani, A.; Wang, X.; Li, Y. C.; Li, F.; Edwards, J.; Richter, L. J.; Thorpe, S. J.; Sinton, D.; Sargent, E. H. CO_2 Electrolysis to Multicarbon Products at Activities Greater than 1 A Cm^{-2}. *Science.* **2020**, *367* (6478), 661–666.

(23) Kroutil, W.; Rueping, M. Introduction to ACS Catalysis Virtual Special Issue on Cascade Catalysis. *ACS Catal.* **2014**, *4* (6), 2086–2087.

(24) Hori, Y.; Takahashi, R.; Yoshinami, Y.; Murata, A. Electrochemical Reduction of CO at a Copper Electrode. *J. Phys. Chem. B* **1997**, *101* (36), 7075–7081.

(25) Pang, Y.; Li, J.; Wang, Z.; Tan, C.-S.; Hsieh, P.-L.; Zhuang, T.-T.; Liang, Z.-Q.; Zou, C.; Wang, X.; De Luna, P.; Edwards, J. P.; Xu, Y.; Li, F.; Dinh, C.-T.; Zhong, M.; Lou, Y.; Wu, D.; Chen, L.-J.; Sargent, E. H.; Sinton, D. Efficient Electrocatalytic Conversion of Carbon Monoxide to Propanol Using Fragmented Copper. *Nat. Catal.* **2019**, *2* (3), 251–258.

(26) Ripatti, D. S.; Veltman, T. R.; Kanan, M. W. Carbon Monoxide Gas Diffusion Electrolysis That Produces Concentrated C2 Products with High Single-Pass Conversion. *Joule* **2019**, *3* (1), 240–256.

(27) Huang, J.; Mensi, M.; Oveisi, E.; Mantella, V.; Buonsanti, R. Structural Sensitivities in Bimetallic Catalysts for Electrochemical CO_2 Reduction Revealed by Ag-Cu Nanodimers. *J. Am. Chem. Soc.* **2019**, *141* (6), 2490–2499.

(28) Morales-Guio, C. G.; Cave, E. R.; Nitopi, S. A.; Feaster, J. T.; Wang, L.; Kuhl, K. P.; Jackson, A.; Johnson, N. C.; Abram, D. N.; Hatsukade, T.; Hahn, C.; Jaramillo, T. F. Improved CO_2 Reduction Activity towards C2+ Alcohols on a Tandem Gold on Copper Electrocatalyst. *Nat. Catal.* **2018**, *1* (10), 764–771.

(29) Zhang, H.; Chang, X.; Chen, J. G.; Goddard, W. A.; Xu, B.; Cheng, M.-J.; Lu, Q. Computational and Experimental Demonstrations of One-Pot Tandem Catalysis for Electrochemical Carbon Dioxide Reduction to Methane. *Nat. Commun.* **2019**, *10* (1), 3340.

(30) Low, Q. H.; Loo, N. W. X.; Calle-Vallejo, F.; Yeo, B. S. Enhanced Electroreduction of Carbon Dioxide to Methanol Using Zinc Dendrites Pulse-Deposited on Silver Foam. *Angew. Chemie - Int. Ed.* **2019**, *58* (8), 2256–2260.

(31) Ren, D.; Ang, B. S.-H.; Yeo, B. S. Tuning the Selectivity of Carbon Dioxide Electroreduction toward Ethanol on Oxide-Derived Cu x Zn Catalysts. *ACS Catal.* **2016**, *6* (12), 8239–8247.

(32) Ren, D.; Gao, J.; Pan, L.; Wang, Z.; Luo, J.; Zakeeruddin, S. M.; Hagfeldt, A.; Grätzel, M. Atomic Layer Deposition of ZnO on CuO Enables Selective and Efficient Electroreduction of Carbon Dioxide to Liquid Fuels. *Angew. Chemie* **2019**, *131* (42), 15178–15182.

(33) Ting, L. R. L.; Piqué, O.; Lim, S. Y.; Tanhaei, M.; Calle-Vallejo, F.; Yeo, B. S. Enhancing CO_2 Electroreduction to Ethanol on Copper-Silver Composites by Opening an Alternative Catalytic Pathway. *ACS Catal.* **2020**, *10* (7), 4059–4069.

(34) Wang, Y.; Wang, D.; Dares, C. J.; Marquard, S. L.; Sheridan, M. V; Meyer, T. J. CO_2 Reduction to Acetate in Mixtures of Ultrasmall $(Cu)_n$, $(Ag)_m$ Bimetallic Nanoparticles. *Proc. Natl. Acad. Sci.* **2018**, *115* (2), 278–283.

(35) Lum, Y.; Ager, J. W. Sequential Catalysis Controls Selectivity in Electrochemical CO_2 Reduction on Cu. *Energy Environ. Sci.* **2018**, *11* (10), 2935–2944.

(36) Gurudayal; Perone, D.; Malani, S.; Lum, Y.; Haussener, S.; Ager, J. W. Sequential Cascade Electrocatalytic Conversion of Carbon Dioxide to C–C Coupled Products. *ACS Appl. Energy Mater.* **2019**, *2* (6), 4551–4559.

(37) Theaker, N.; Strain, J. M.; Kumar, B.; Brian, J. P.; Kumari, S.; Spurgeon, J. M. Heterogeneously Catalyzed Two-Step Cascade Electrochemical Reduction of CO_2 to Ethanol. *Electrochim. Acta* **2018**, *274*, 1–8.

(38) Babu, P. K.; Chung, J. H.; Oldfield, E.; Wieckowski, A. CO Surface Diffusion on Platinum Fuel Cell Catalysts by Electrochemical NMR. *Electrochim. Acta* **2008**, *53* (23), 6672–6679.

(39) Nilekar, A. U.; Greeley, J.; Mavrikakis, M. A Simple Rule of Thumb for Diffusion on Transition-Metal Surfaces. *Angew. Chemie Int. Ed.* **2006**, *45* (42), 7046–7049.

(40) Cheng, T.; Xiao, H.; Goddard, W. A. Reaction Mechanisms for the Electrochemical Reduction of CO_2 to CO and Formate on the Cu(100) Surface at 298K from Quantum Mechanics Free Energy Calculations with Explicit Water. *J. Am. Chem. Soc.* **2016**, No. 100, jacs.6b08534.

(41) Lum, Y.; Ager, J. W. Evidence for Product-Specific Active Sites on Oxide-Derived Cu Catalysts for Electrochemical CO_2 Reduction. *Nat. Catal.* **2019**, *2* (1), 86–93.

(42) Hahn, C.; Hatsukade, T.; Kim, Y.-G.; Vailionis, A.; Baricuatro, J. H.; Higgins, D. C.; Nitopi, S. A.; Soriaga, M. P.; Jaramillo, T. F. Engineering Cu Surfaces for the Electrocatalytic Conversion of CO_2 : Controlling Selectivity toward Oxygenates and Hydrocarbons. *Proc. Natl. Acad. Sci.* **2017**, *114* (23), 5918–5923.

(43) Montoya, J. H. H.; Shi, C.; Chan, K.; Nørskov, J. K. K. Theoretical Insights into a CO Dimerization Mechanism in CO_2 Electroreduction. *J. Phys. Chem. Lett.* **2015**, *6* (11), 2032–2037.

(44) Wu, B.; Kumar, A.; Pamarthy, S. High Aspect Ratio Silicon Etch: A Review. *J. Appl. Phys.* **2010**, *108* (5), 051101.

(45) Lobaccaro, P.; Singh, M. R.; Clark, E. L.; Kwon, Y.; Bell, A. T.; Ager, J. W. Effects of Temperature and Gas-Liquid Mass Transfer on the Operation of Small Electrochemical Cells for the Quantitative Evaluation of CO_2 Reduction Electrocatalysts. *Phys. Chem. Chem. Phys.* **2016**, *18* (38), 26777–26785.

(46) Roldán Cuenya, B.; Scholten, F.; Nguyen, K.-L. C.; Bruce, J. P.; Heyde, M. Identifying Structure-Selectivity Correlations in the Electrochemical Reduction of CO_2: Comparison of Well-Ordered Atomically-Clean and Chemically-Etched Cu Single Crystal Surfaces. *Angew. Chemie Int. Ed.* **2021** Accepted Author Manuscript. https://doi.org/https://doi.org/10.1002/anie.202103102.

(47) Xi, W.; Ma, R.; Wang, H.; Gao, Z.; Zhang, W.; Zhao, Y. Ultrathin Ag Nanowires Electrode for Electrochemical Syngas Production from Carbon Dioxide. *ACS Sustain. Chem. Eng.* **2018**, *6* (6), 7687–7694.

(48) Zhang, H.; Zhang, Y.; Li, Y.; Ahn, S.; Palmore, G. T. R.; Fu, J.; Peterson, A. A.; Sun, S. Cu Nanowire-Catalyzed Electrochemical Reduction of CO or CO_2. *Nanoscale* **2019**, *11* (25), 12075–12079.

(49) Gupta, N.; Gattrell, M.; MacDougall, B. Calculation for the Cathode Surface Concentrations in the Electrochemical Reduction of CO_2 in $KHCO_3$ Solutions. *J. Appl. Electrochem.* **2006**, *36* (2), 161–172.

TABLE OF CONTENTS (TOC) IMAGE

